Int. J. Solids Structures Vol. 26, No. 9/10, pp. 1071–1098, 1990
Printed in Great Britain.

0020–7683/90 $3.00 + .00
Pergamon Press plc

AN EXPERIMENTAL STUDY OF COMPRESSION FAILURE OF FIBROUS LAMINATED COMPOSITES IN THE PRESENCE OF STRESS GRADIENTS

A. M. WAAS,† C. D. BABCOCK, JR‡ and W. G. KNAUSS
Division of Engineering and Applied Science, Caltech, Pasadena, CA 91125, U.S.A.

Abstract—A series of experiments have been performed to determine the mechanisms of failure in compressively loaded laminated plates in the presence of stress gradients generated by a circular cutout. Real-time holographic interferometry and *in situ* photomicrography of the cutout surface are employed to observe the progression of failure.

The test specimens are multi-layered composite flat plates which are loaded in compression. The plates are made up of two material systems, T300/BP907 and IM7/8551-7. Two different lay-ups of T300/BP907 and four different lay-ups of IM7/8551-7 are investigated.

The experimental results reveal that the failure is initiated as a localized instability in the 0° plies at the hole surface approximately at right angles to the loading direction. This instability which emanates at the hole edge and propagates into the interior of the specimen within the 0° plies, involves fiber microbuckling. Subsequent to the 0° ply failure, extensive delamination cracking is observed with increasing load. The delaminated portions spread to the undamaged areas of the laminate by a combination of delamination buckling and growth, the buckling further enhancing the growth. When the delaminated area reaches a critical size, about 75–100% of the hole radius in extent, an accelerated growth rate of the delaminated portions is observed. The culmination of this last event is the complete loss of flexural stiffness of each of the delaminated portions leading to catastrophic failure of the plate.

1. INTRODUCTION

The use of graphite/epoxy laminates in various fields of engineering has posed a new challenge to engineering design. In particular, it is necessary to explore new techniques to characterize these materials which differ in their response to mechanical load from isotropic, homogeneous materials.

One situation in which these laminates exhibit a different type of behavior is under compressive loads. One or several competing modes of failure can be present and the researcher is thus left with the task of identifying the most important features of the failure process for design purposes. When structural components are made out of these laminates it is seldom that they will persist in an environment free of stress concentrations. Stress raisers can be very detrimental, and are the sites where damage can initiate in a structure.

The strengths of these laminates in the presence of holes or cutouts has been the subject of numerous investigations (Starnes and Williams, 1982; Rhodes *et al.*, 1982; Shuart and Williams, 1986; Knauss *et al.*, 1978). Figure 1 illustrates the ultimate load-carrying capacity of such laminates as a function of the normalized hole diameter. Mikulas (1980) has shown that these results could be bounded by simple criteria based on notch sensitivity. If the material is notch insensitive, the failure strains are directly proportional to the reduction in cross-sectional area, while if the material is notch sensitive it is postulated that the material fails when the strain concentration at the hole edge equals the failure strain of the material. It is seen that the latter assumption is too conservative in that the failure strain is underestimated for (**a**/**w**) ratios less than 0.4. This situation indicates the possibility that the strain concentration effect alone cannot account for the failure process and that a localized failure mechanism may be present. Based on this premise Starnes and Williams (1982) carried out open hole strength testing of laminates and reported a shear crippling type of failure to be prevalent in the vicinity of the hole prior to catastrophic failure. This conclusion was based on *post mortem* examination of damaged specimens.

† Present address: Department of Aerospace Engineering, University of Michigan, Ann Arbor, MI 48109, U.S.A.

‡ Deceased. Formerly, Professor of Aeronautics and Applied Mechanics.

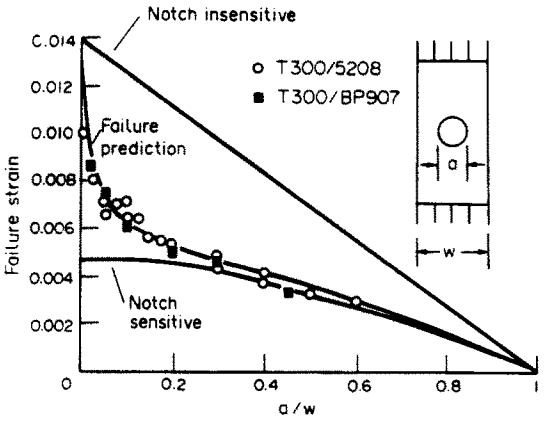

Fig. 1. Summary of test results for T300/BP907 and T300/5208 composite laminates, $w = 13$ cm (from Starnes and Williams, 1982).

In these and other similar investigations no attempt has been made to follow the progression of failure in detail. The progressive nature of failure, through various stages is often a characteristic property of laminated composites. Several different failure processes can be prevalent when laminates are stressed and it is thus necessary to identify the key aspects of failure in a particular situation.

Motivated from such an understanding, the present paper, which is condensed from Waas (1988) describes a detailed experimental investigation to understand the initiation and propagation of failure in laminates in the presence of a stress raiser. The stress concentration effect is produced by choosing a flat plate with a centered circular hole and subjecting it to an in-plane compressive load. The hole is carefully cut in order to insure that excessive local damage does not occur during the machining process. The damage initiation and propagation throughout the entire load history is studied via real-time holographic interferometry and photomicrography of the hole surface. The results are substantiated by post experiment ultrasonic examination of the damaged specimens and by means of an optical microscope.

In the sections to follow, the experiments and associated methodology are presented first. Pertinent details are given where necessary, but the interested reader is referred to relevant texts on holography, ultrasonic scanning etc. for a detailed treatment of the subjects. It must be emphasized that the main goal of this investigation is not a systematic study of the stress gradient effect on the failure of the laminates, but rather, having chosen a geometry that produces stress gradients, to identify the mechanisms of failure.

2. THE EXPERIMENT

2.1. *Assembly*

Figure 2 is a photograph showing the arrangement of the various devices used in the experiment. On a pneumatically vibration isolated table, optical components are arranged to make a hologram and generate interferograms of the test specimen which is loaded by a table top compression device. An optical microscope is mounted on a tripod which is situated adjacent to the optical table by the testing machine. A 35 mm motor driven SLR camera attached to the microscope is used to record photographs of the test specimen hole surface, during the testing sequence. Recording and developing of the hologram is accomplished on a thermoplastic plate which is housed in the body of the instant recording device (IRD) as marked in Fig. 2. This device, which is electronically controlled, replaces the conventional wet chemical processes associated with normal photographic plates. A video camera placed behind the thermoplastic plate views the test specimen through the hologram. A VCR records the interferometric patterns generated during the loading sequence. A TV monitor is used to view the interferograms during a typical test, so as to

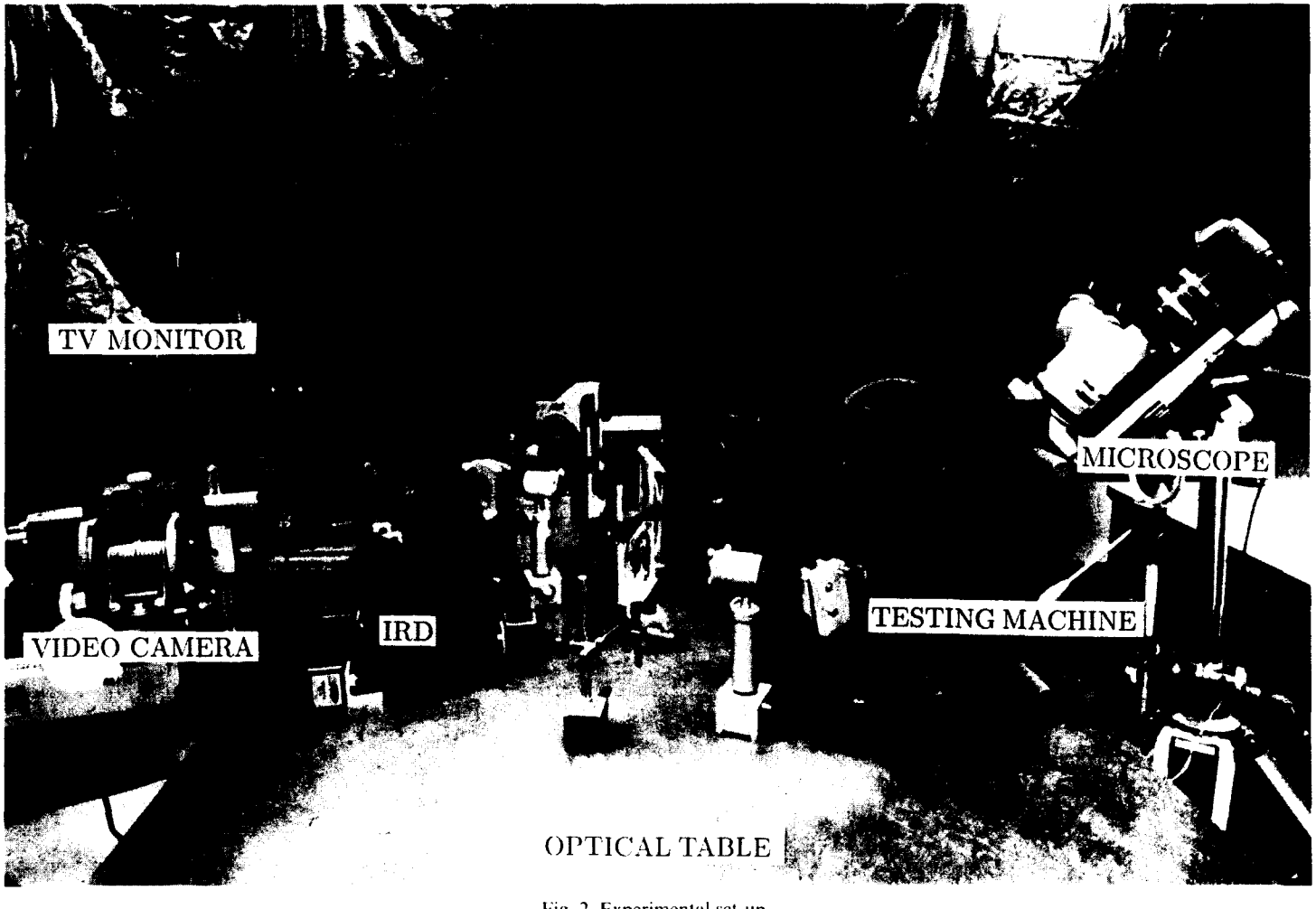

Fig. 2. Experimental set-up.

Table 1. Laminate configurations

Specimen type	Stacking sequence
A	$(+45/-45/0_2/+45/-45/0_2/+45/-45/0/90)_{2s}$
B	$(-45/+45/90_2/-45/+45/90_2/-45/+45/90/0)_{2s}$
C	$(+45_6/-45_6/0_6/90_6)_s$
D	$(-45_6/+45_6/90_6/0_6)_s$

allow performance of the test "interactively". In the following sections the main components of the experiment are described.

2.2. *Specimens*

The multi-layered laminated plates used in the tests were supplied by NASA Langley Research Center. The composition of the laminae in the specimens consisted of Thornel-300 graphite fibers pre-impregnated with American Cyanamide BP907 epoxy resin, and IM7 graphite fibers preimpregnated in 8551-7 epoxy resin. The IM7 fibers have a smaller diameter (5 μm) than the T300 fibers (7 μm). The fiber volume fraction in both these systems is 0.5–0.6. These laminates are typical of those used in the aerospace industry. Four types of lamina stacking sequences were used in the tests. The first designated type A contains 48 plies in the sequence $[45/-45/0/0/+45/-45/0/0/+45/-45/0/90]_{2s}$ while the other, type B, is obtained by rotating the first sequence by 90°, the angles being measured counterclockwise with respect to the loading direction. Type C is configured from 48 plies according to $[+45_6/-45_6/0_6/90_6]_s$, while type D is obtained by rotating type C in the manner described before for types A and B. Table 1 summarizes the laminate types. Diamond-impregnated core drills and saws are used for machining the specimens. Two sizes of specimens are used. The first designated "S" (small) is 7.62 cm × 10.2 cm and the other "L" (large) is 12.7 cm × 15.3 cm.

2.3. *Testing machine*

The use of real-time holographic interferometry requires vibration isolation of the test specimen and testing device. To that end, a special purpose testing device was designed and constructed, so that both tension and compression load can be applied. At the commencement of a test one end of the specimen support holder is inserted into an adapter which threads onto the actuator arm of the loading device. A ball joint is attached to the other end. The mating part of the ball joint is positioned at the center of a 445 kN (100,000 lbf) load cell. The load cell is mounted on one of the flanged box beams of the testing machine. The load–time history is regulated through a servo controlled loading mechanism. The servo valve and associated accessories are mounted on a plate which fits on the cylinder of the loading device. A function generator is used to program the loading path.

2.4. *Holographic interferometry*

Real-time holographic interferometry is used in this study to record the out-of-plane displacement changes Δw of the specimen during the loading sequence. The relevant details of the technique as applicable to the present experiment are given in Section 2.6. As mentioned before, the recording of a hologram was accomplished in a special device marketed by Newport Research Corporation—as opposed to normal photographic plates. The time consumed during the wet-photographic process is about 7–9 min, and is a significant portion of the total duration of a test, which lasts on the order of 2 hours. During a continuous loading sequence, the information on the displacement history is lost during this development time. The electronic process referred to above and explained in the next section overcomes this drawback.

2.5. *The instant recording device*

In the reconstruction process of a hologram the conventional silver halide photographic plates cause diffraction via an amplitude grating which is representative of the spatial distribution of light (amplitude and phase) that is emitted from the diffusely reflective

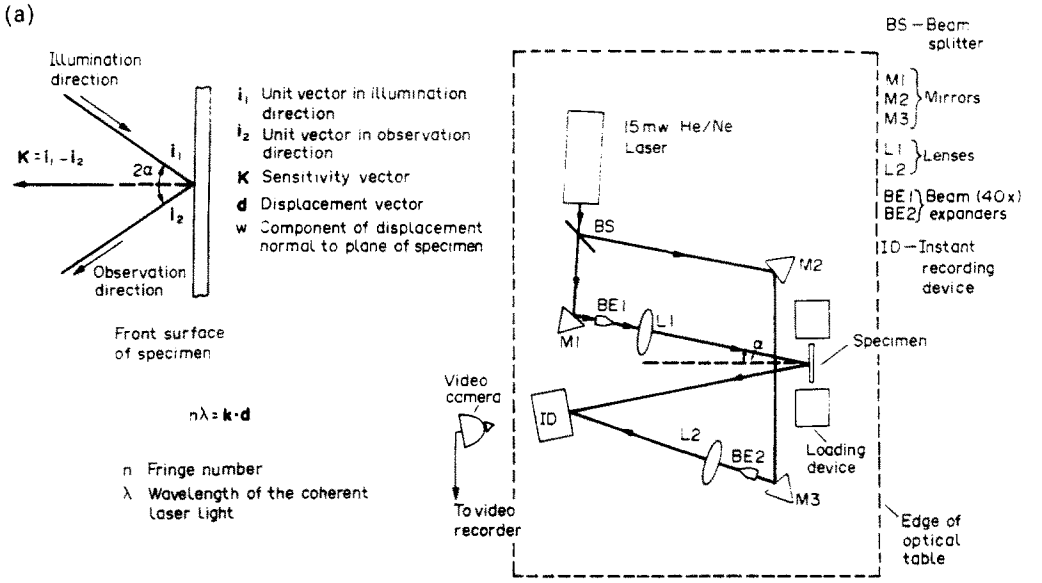

Fig. 3(a). Holographic interferometer and details.

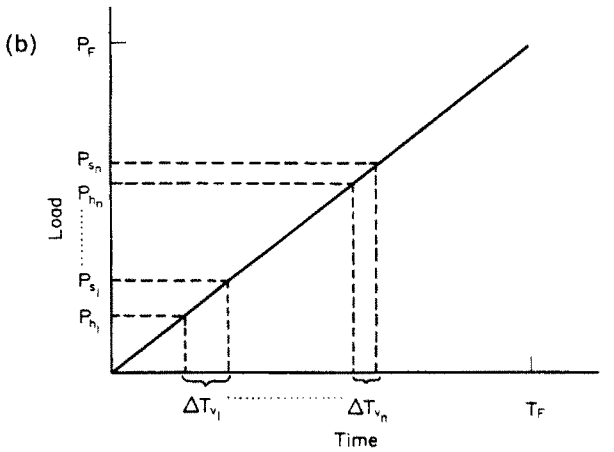

P_h – Load at which hologram is made

P_s – Load at which fringe resolvability is poor

ΔT_v – Viewing duration for each interferogram sequence

P_F – Maximum load sustained by specimen

T_F – Duration of test

Fig. 3(b). Experimental procedure for generating holographic interferograms.

surface of the object. However, the same task could be accomplished with a phase grating, i.e. a surface contour variation which is representative of the light off the object. This is the basic idea behind the success of the thermoplastic recording device. The device has several stages of operation as detailed in the Owners Manual (1986).

2.6. *Experimental procedure*

A schematic of the holographic interferometer used in this study is shown in Fig. 3(a). It is a standard off-axis holographic system. Proper choice of reference to object beam intensity ratio is important for producing the best holograms. With the use of the instant

recording device, the quality of the hologram is insensitive to the exposure time. In the real-time mode, the test specimen is illuminated in a state, say S_1, with coherent light transmitted from the laser via the object wave path. This path contains the beam splitter, a beam expander–spatial filter, and a collimating lens. The corresponding load is P_1 [refer to Fig. 3(b)]. A hologram is then recorded by exposing the thermoplastic plate positioned at the junction of the reflected light and reference beam. Upon completion of the first exposure, the specimen, which is continuously loaded, is viewed through a camera attached to a VHS recording system (a VCR and a monitor). The resulting image consists of fringes which are dynamical in nature representing contour maps of the changes in the out-of-plane displacement component w of the specimen, with respect to the state S_1. These fringes, together with the load cell reading are recorded. The load cell reading is obtained by focusing the display of the voltmeter, exhibiting the load cell reading, at the position of the circular hole in the plane of the test specimen. With increasing load on the specimen the fringe density becomes high, so that the resolution of the interferogram becomes poor. At this stage a new hologram of the test specimen is made and the above cycle of events is repeated. Thus, at the end of each experiment we obtain an interferometric record of the complete out-of-plane displacement history of the specimen as well as the corresponding loading.

Each of the holographic interference fringe fields is related to the change in surface displacement of the specimen under load, by the vector expression

$$n\lambda = \mathbf{k} \cdot \mathbf{d} \tag{1}$$

where,

- n fringe number
- λ wavelength of the coherent laser light
- $\mathbf{k}$ sensitivity vector $(\mathbf{i}_2 - \mathbf{i}_1)$
- $\mathbf{d}$ surface displacement vector at point of observation.

Here $\mathbf{i}_1$ and $\mathbf{i}_2$ are the unit vectors in the illumination and observation directions, respectively. In the present experimental set-up the diffusely reflective surface of the specimen is oriented normal to the bisector of the angle 2α, between $\mathbf{i}_1$ and $\mathbf{i}_2$ [Fig. 3(a)]. Thus, since the sensitivity vector $\mathbf{k}$ also points along this bisector, the interferometer senses only the out-of-plane displacement component w. Equation (1) then becomes

$$n\lambda = 2w \cos \alpha$$

or,

$$w = \frac{n\lambda}{2 \cos \alpha}. \tag{2}$$

In the present experimental set-up, the surface normal makes an angle of 10° with the observation direction. With $\lambda = 0.633$ μm, eqn (2) computes that each fringe represents an out-of-plane displacement change of 0.321 μm.

During the entire loading program, the surface of the hole is viewed through a microscope at an oblique angle and photographs are taken at various times. Due to the oblique viewing angle, the hole surface appears curved on the photomicrographs. A fiber optic cable attached to a high intensity lamp is used to illuminate the hole surface. The interferograms displayed on the TV monitor assist in taking these photomicrographs interactively.

The interferometric data indicate the changes in the out-of-plane displacement component, which changes may be manifestations of internal damage. Thus, some specimens were loaded past the damage initiation level but were unloaded prior to catastrophic failure. The unloaded specimens were sectioned in the region of stress concentration and were examined under an optical microscope. In the following section the results obtained from interferometry, photomicrography and interior damage studies are presented.

Table 2. Experimental results for T300/BP907 laminates

Specimen type	Hole dia. (cm)	Thickness (mm)	P_i(KN)	P_f(KN)
TB1-AS	2.54	7.51	126.0	127.0†
TB2-AS	2.54	7.51	124.0	125.0†
TB10-AS	2.54	7.53	124.0	127.0
TB12-AS	2.54	7.53	125.0	127.0
TB7-BS	2.54	7.51	64.0	91.0
TB13-BS	2.54	7.47	69.0	90.0
TB6-BL	2.54	7.51	127.0	168.0
TB11-BL	2.54	7.53	123.0	165.0‡
TB9-BL	2.54	7.51	119.0	169.0
TB14-AS	1.90	7.47	130.0	142.0
TB17-AS	1.90	7.53	128.0	143.0‡
TB16-BS	1.90	7.47	70.0	97.0‡
TB18-BS	1.90	7.53	79.0	110.0
TB15-AS	1.27	7.47	152.0	161.0

† Load held constant after initiation.
‡ Maximum load sustained. Specimen unloaded for microscopic examination.

3. RESULTS AND DISCUSSION

Tables 2 and 3 summarize the test conditions and the results obtained. In these tables, "AS" for example, refers to type "A", small. P_i is the load at which failure initiates, as detected by the interferometer. P_f is the ultimate failure or collapse load. Figures that contain interferometric data are presented only in the immediate neighborhood of the hole [for example, see Fig. 4(a)]. The photomicrographs are only captured on one side of the hole surface. In Fig. 5, for example, the horizontal shiny stripes appearing on the photomicrographs are 0° plies while vertical lines are pencil marks for purposes of reference.

We consider next the different stages of failure as traced via the interferometry and as substantiated by the photomicrographs. In the pre-damaged state an increase in the load on the specimen results in a uniform pattern of fringes. These fringes are few in number and correspond to the thickness changes due to the Poisson effect, but coupled with some rigid body motion and/or slight bending. The rigid body motion and the bending cannot be totally avoided in a compression test. The slight bending may be the result of any initial imperfection in the specimen. One should also be mindful of the high sensitivity of the measurement technique which is a function of the wavelength of the laser light. We turn next to a discussion of the mechanisms of the failure process that is common to all the laminate types. Certain differences are then pointed out and summarized at the end of this paper. For ease of presentation, the T300/BP907 material system will be referred to as "TB", while the IM7/8551-7 will be referred to as "IM". In the following discussion, the results pertaining to type B specimens are presented first, as they elucidate certain features that are common to the different laminates (types A, B, C and D as designated in Table 1).

3.1. *Type B specimens*

This type of specimen is one in which there are a fewer number of 0° plies (8.3%). Figure 4a shows a series of interferometric patterns, which correspond to the first instance at which internal damage was detected. The numbers below each picture represent the load in kiloNewtons (1 kN ≡ 224.8 lbf) corresponding to each frame, while P_h indicates the load at which the hologram was made for that particular set of frames (reference load). Notice the highly localized fringe cluster adjacent to the hole edge at approximately 90° to the loading direction. This pattern is typical whenever internal damage occurs to manifest itself as a localized perturbation in the laminate normal displacement w. A view of the hole surface corresponding to this fringe pattern is shown in the second frame of Fig. 5. Notice the damage to the midplane 0° plies which appears as a black spot. Adjacent to this and below in that figure is a delamination crack. Inspection of photomicrographs prior to this event revealed no damage to the hole surface. In all experiments it was apparent that a

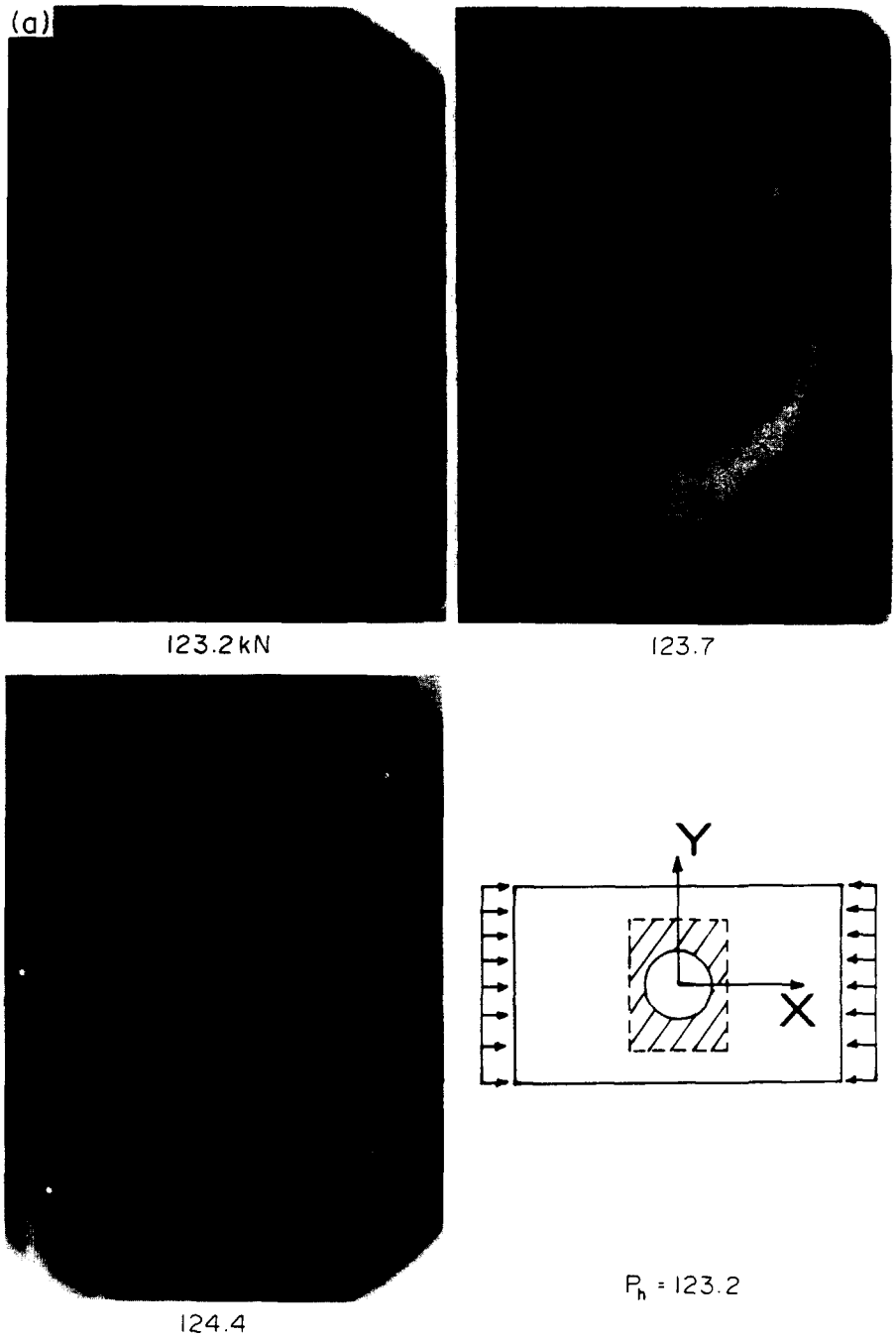

Fig. 4(a). Initiation of damage (specimen TB11).

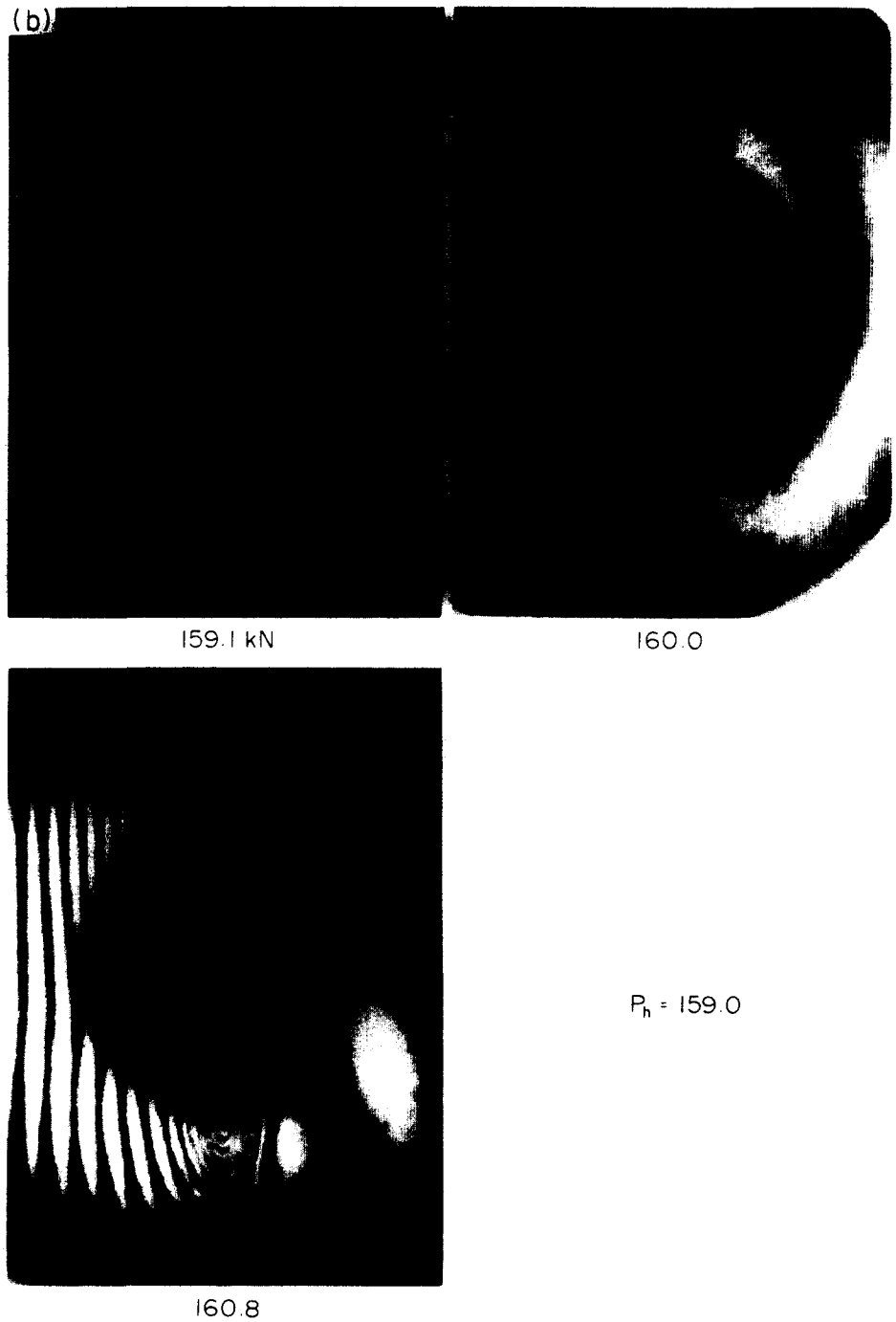

Fig. 4(b). Buckling and spreading of delaminated portions (specimen TB11).

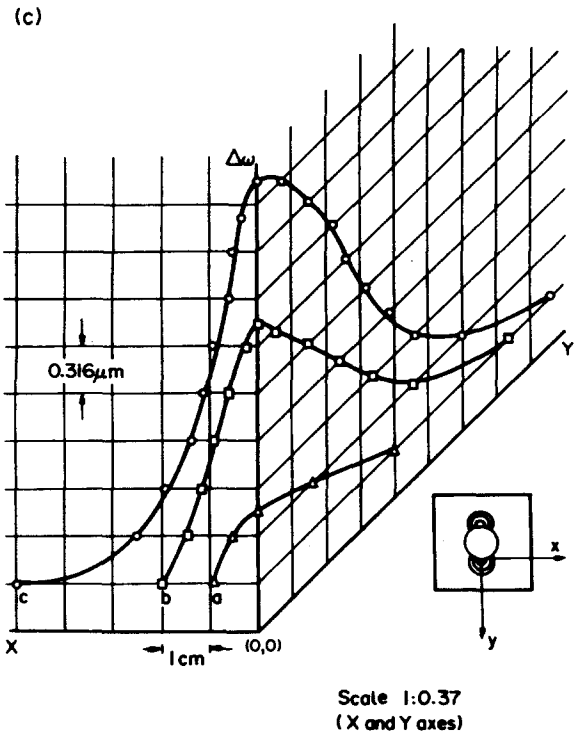

Fig. 4(c). Summary of displacements corresponding to Fig. 4(b).

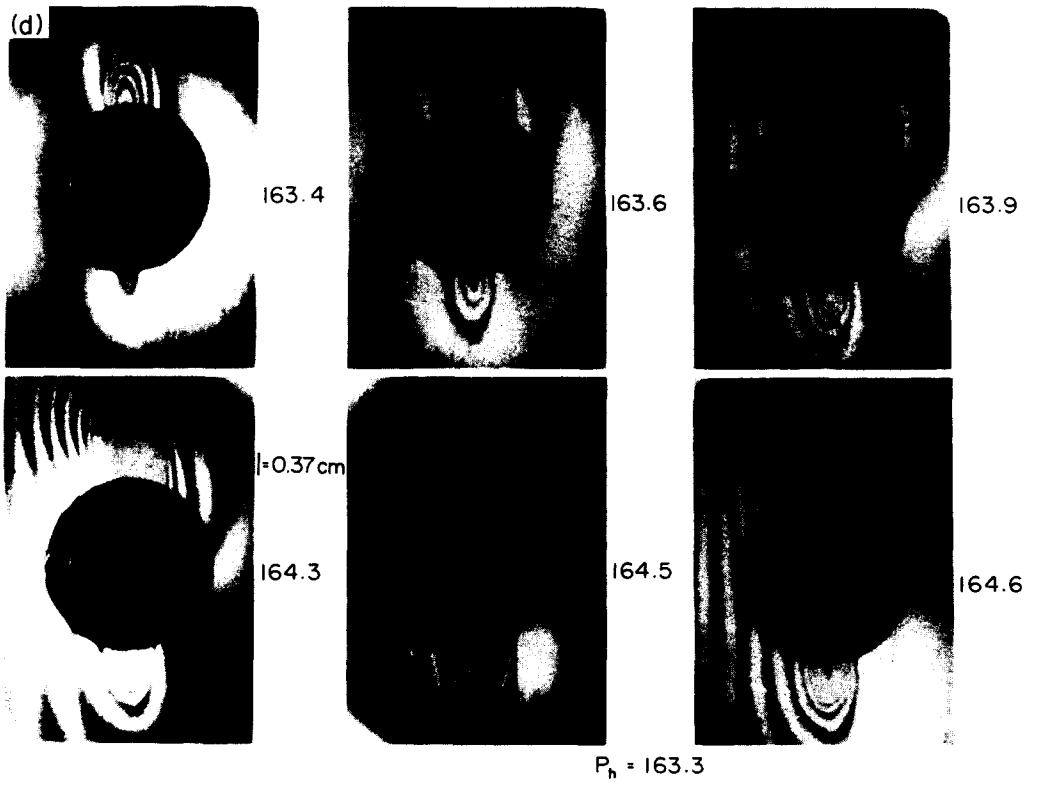

Fig. 4(d). Buckling and spreading of delaminated portions just prior to catastrophic failure (specimen TB11).

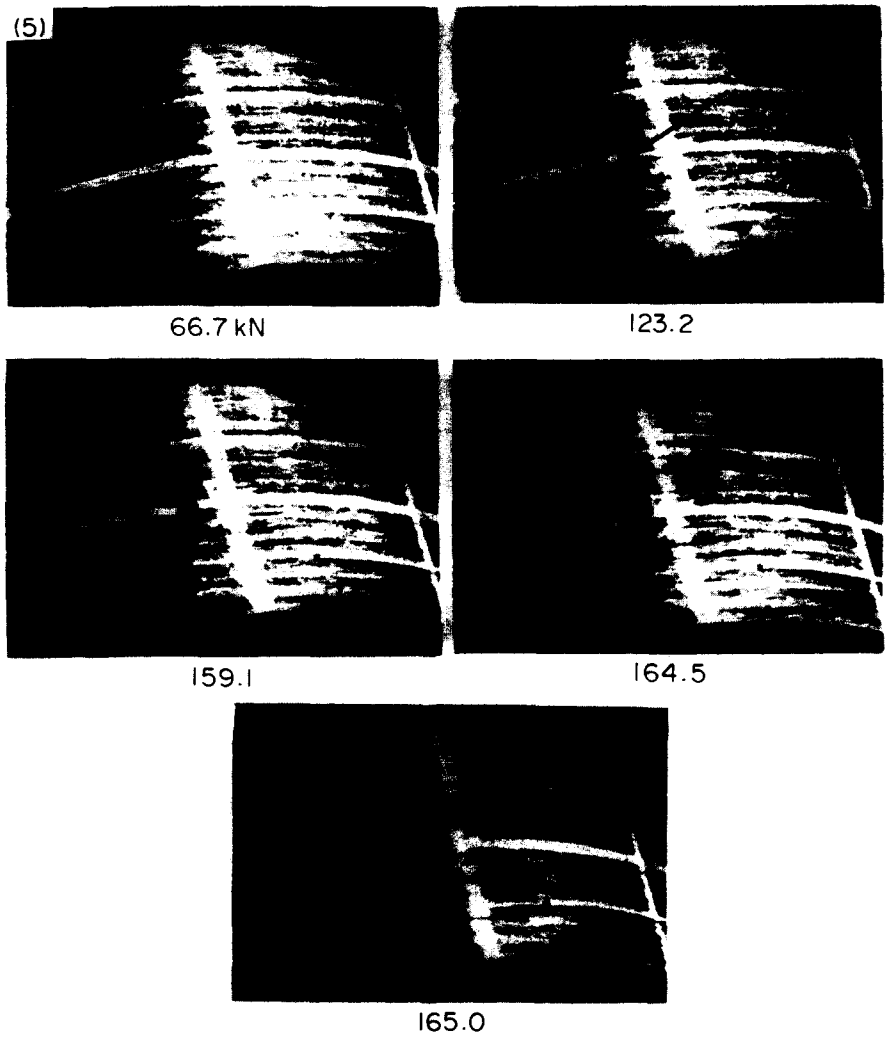

Fig. 5. Hole surface photomicrographs of specimen TB11 (type B). Arrow points to location of initial damage.

Table 3. Experimental results for IM7/8551-7 laminates

Specimen type	Hole dia. (cm)	Thickness (mm)	P_i(KN)	P_f(KN)
IM2-AS	2.54	7.44	128.5	144.1
IM4-AS	2.54	7.31	135.7	141.9
IM5-AS	2.54	7.33	124.8	129.0
IM7-AS	2.54	7.33	125.0	133.2
IM16-AS‖	2.54	7.32	119.2	128.3
IM20-AS	2.54	7.36	127.7	132.8
IM21-AS‖	2.54	7.32	125.0	134.3
IM29-AS	2.54	7.32	125.9	133.2
IM1-BS	2.54	7.38	68.7	97.8
IM3-BS	2.54	7.32	72.0	88.3
IM6-BS	2.54	7.36	70.5	92.1
IM8-BS‖	2.54	7.36	67.2	89.4
IM9-BS‖	2.54	7.33	72.1	89.8
IM19-BS‖	2.54	7.36	68.9	76.3
IM32-BS	2.54	7.30	60.0	90.3
IM24-BL‖	2.54	7.36	127.0	136.3
IM25-BL‖	2.54	7.44	123.2	165.5
IM28-BL	2.54	7.33	114.3	164.1
IM11-CS	2.54	7.38	83.0	91.0
IM13-CS	2.54	7.36	87.2	91.6
IM15-CS‖	2.54	7.31	81.8	91.2
IM18-CS	2.54	7.38	88.5	93.0
IM31-CS	2.54	7.36	85.0	92.7
IM22-CL†‖	2.54	7.36	—	135.7
IM26-CL	2.54	7.33	143.0	164.6
IM10-DS	2.54	7.38	72.5	87.6
IM12-DS†	2.54	7.25	74.3	95.0
IM14-DS†	2.54	7.36	75.4	90.3
IM17-DS‖	2.54	7.28	75.6	79.4
IM30-DS§	2.54	7.28	76.5	82.3
IM23-DL‖	2.54	7.33	128.8	150.1
IM27-DL	2.54	7.28	136.6	147.0

† Failure initiated at the hole surface with no indication of propagation. Final failure occurred abruptly.

‡ Specimen unloaded prior to indication of failure initiation.

§ Transients in the power lines driving the servo-controller led to premature initiation.

‖ Maximum load sustained. Specimen unloaded for microscopic examination.

perturbation in the interferometric data corresponded to always 0° ply damage at the hole surface. This localized damage to the 0° plies triggers extensive delamination cracking and causes localized buckling of the delaminated portions. The interferograms corresponding to the initiation event indicate that the displacements within the damage zone increase with increasing load as evidenced by a clear and monotonic increase in the fringe density as loading proceeds. Subsequent to the initiation, the remaining 0° plies undergo failure while delaminations are seen to appear between various ply interfaces, as an inspection of the photographic sequence in Fig. 5 shows.

The delaminations then undergo a stage of slow growth as shown in the next set of interferometric patterns of Fig. 4(b). Here the reference state corresponds to a load $P_h = 159$ kN while the three frames span a load increase of ΔP of 1.73 kN. The displacement patterns extracted from the interferograms in Fig. 4(b) are shown in Fig. 4(c). Here the displacements are measured with respect to those in areas remote from the hole edge. The origin of the axes is placed at the edge of the hole as indicated in that figure. The X and Y axes are scaled while the vertical Z axes representing Δw is 1:1. The fringe patterns in Fig. 4(b) indicate that the displacement w grows faster within the damage zone than in the rest of the specimen. Further, the extent of damage is also seen to grow, indicating that the delaminated portions are spreading outward approximately normal to the direction of applied load as shown in Fig. 4(b). The photomicrographs of Fig. 5 indicate 0° fiber breaks as well as the large lateral displacements of the plies which are on the order of a ply thickness. These observations

lead us to conclude that delamination buckling is the mechanism responsible for spreading of the damage into the plate.

Once the delaminated portions reach a sizeable extent an increase in the growth rate is noticed. This is shown in the series of interferograms in Fig. 4(d). While the fringe density within the damage zone is so high that the resolution within this area is poor, one can determine the manner in which these delaminations grow by following the fringe development within the damage area. In this connection it must be pointed out that playback of the recorded video information displays this continuous development in the fringe data; thus there is no need to rely on the limited number of frames displayed here. The culmination of the last growth event is the loss of flexural stiffness of each of the delaminated portions, leading to catastrophic failure.

To study the development of the 0° ply damage further, some specimens were loaded into the post-initiation level but unloaded prior to catastrophic failure. In particular, the specimen represented in Fig. 4 was unloaded from near its ultimate failure and sectioned for further study. An enlarged view of the black spot appearing in the photomicrographs of Fig. 5 is shown in "A" of Fig. 6(b). Notice that a part of the picture is out of focus. The reason is that the fibers in that region have jutted out of the plane of the hole surface (plane of the picture). Examination of similar damage to other 0° layers revealed the same type of jutout failure.

It was also of interest to determine the extent to which the damage sustained at the hole surface propagated into the interior of the specimen. Therefore, the laminate was sectioned at different locations as indicated in Fig. 6(a). Magnified views of the 0° plies at sections "A", "B", "C" and "D" are shown in Fig. 6(b). Notice the dark regions in "B" showing broken fiber segments scattered at different angles. In "C" and "D" an undamaged portion of the midplane 0° layer is shown contrasted against a damaged portion which indicates a characteristic V-shaped pattern. In this region the fibers have undergone rotations, and to a large extent, fracture at the boundary. The maximum width of the V-shaped zone measures approximately 0.3 mm and the "legs" are inclined at an angle of 65° to the 0° fiber direction. These types of failure patterns have been characterized in the

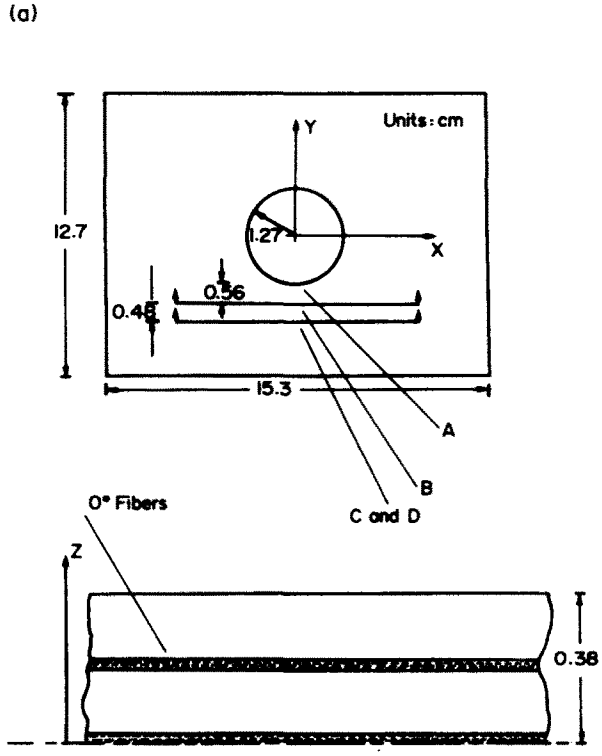

Fig. 6(a). Post experiment microscopic examination (specimen TB11).

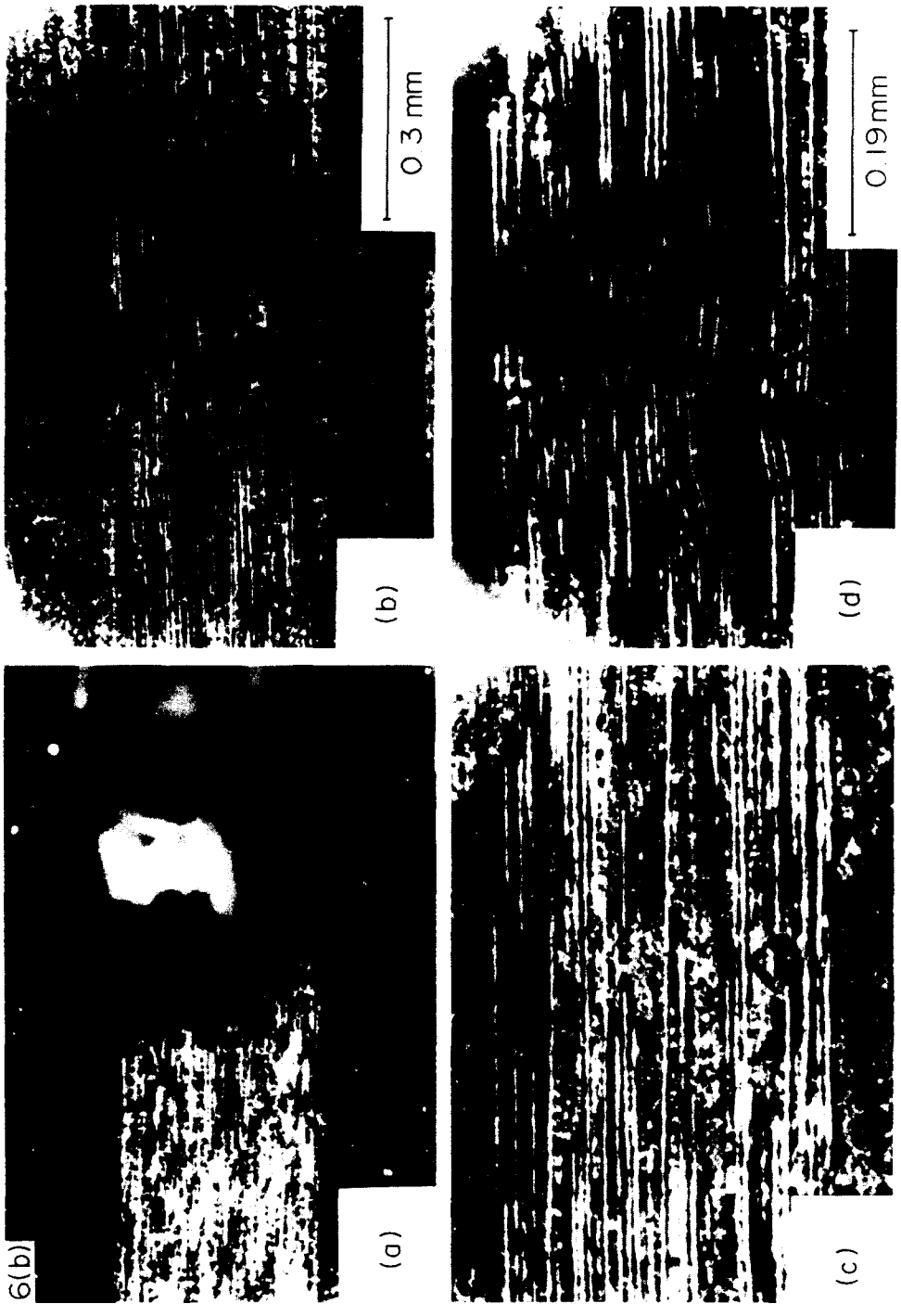

Fig. 6(b). Surface internal damage to specimen TB11 at difference cross-sections.

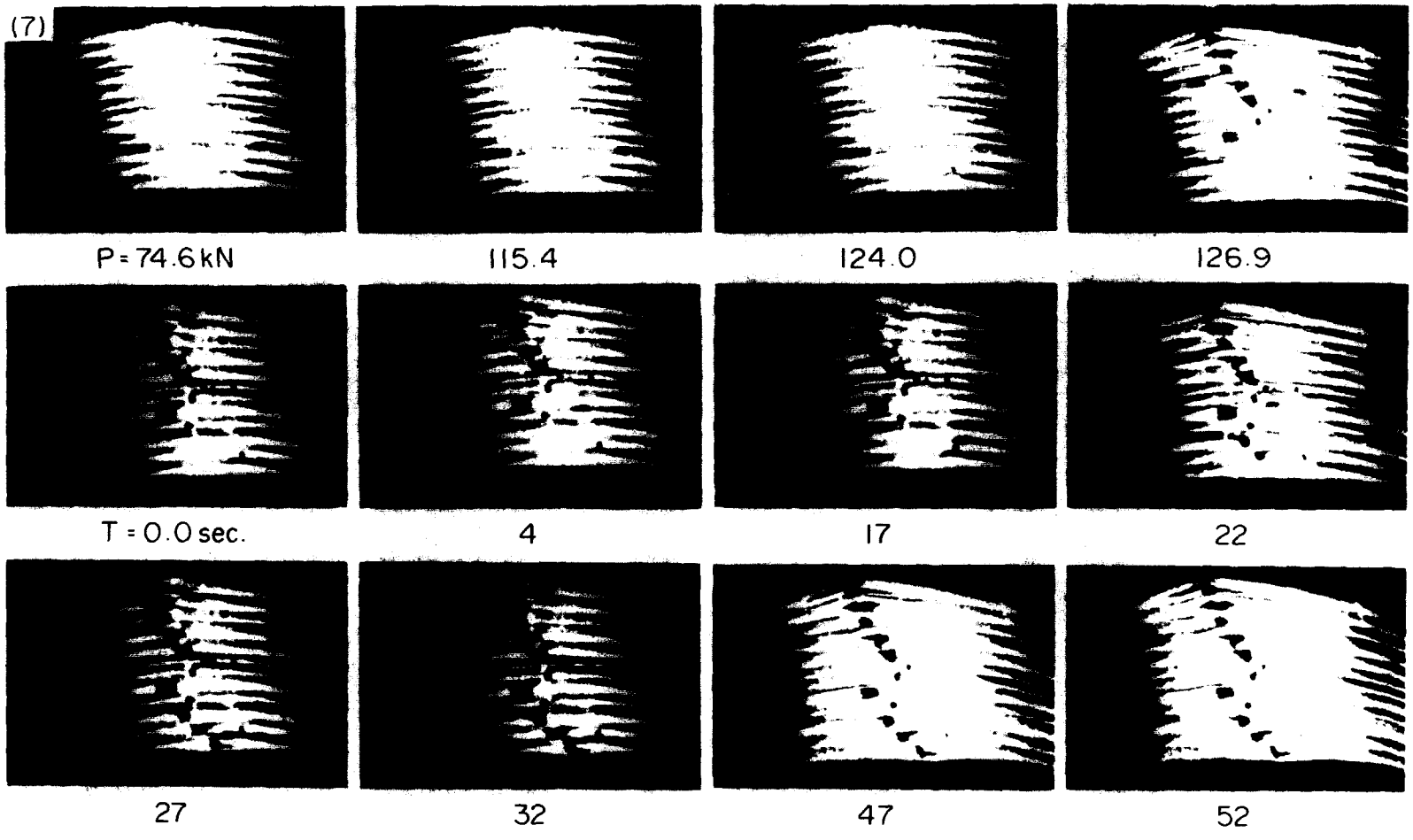

Fig. 7. Hole surface photomicrographs of specimen TB10 (type A).

literature collectively by fiber kinking. Kinking failure has also been observed in other studies investigating the compressive strength of laminates (Pfaff, 1986; Evans and Adler, 1977; Chaplin, 1977; Budiansky, 1983).

Sectioning beyond cross-section "D" and inspection under the microscope revealed no further damage. Similar inspection on other specimens loaded to levels just short of catastrophic failure revealed that the damage zone was contained within a domain that extends out a distance of about one hole radius from the edge of the hole.

3.2. *Type A specimens*

These specimens have a larger number of 0° layers (42%) than type B. The mechanisms leading to failure initiation and propagation for this type of specimen are the same as discussed for the type B specimens, except that the levels of applied load at which the pertinent events take place are different. This is illustrated in Tables 2 and 3. Typically, a sharp localized cluster of fringes form at the edge of the hole which spread very rapidly with a small increase in applied load. The area in which the fringes are unresolvable extends out to about 80% of the hole radius, from the hole edge. A corresponding set of photomicrographs, typical of these specimens, is shown in Fig. 7. In these, the first 0° fiber failure occurs at 124 kN, and is shown in the third frame of the montage of pictures. The fourth frame corresponds to several zero-ply failures and the formation of a surface buckle. The fifth frame is designated the time $T = 0$ s. The subsequent time progression of failure leading to catastrophic collapse is shown in the following series of frames (corresponding to a constant load of ≈ 127 kN) where the numbers below each frame denote the time in seconds measured with respect to frame 4. The final disintegration of the specimen occurs within about 1 min subsequent to frame 5. Notice the damage to all 0° plies at that stage and the formation of surface buckles on both flat surfaces of the specimen.

In the interferometric sequences discussed so far it was found that fringe resolvability was less than desirable close to the hole surface. This is so because the pictures are displayed on a TV monitor and then photographed. The thermoplastic plate has a resolution at maximum diffraction efficiency of 800 lines mm^{-1} [or 2400 lines full screen assuming no spatial variation (Owners Manual, 1986)] but the resolution of the optical system is controlled by the component with the poorest resolving capability, the VCR, which is capable of retaining only 240 lines per frame. At maximum fringe density this is a reduction by a factor of 100. However, in practice, speckle size and other limitations have to be accounted for, too, in order to determine a reasonable measure for this reduction factor (Vest, 1979; Pfaff, 1986). Thus, for high fringe densities, some picture quality is lost. To check the regions of high fringe density, the recording procedure was modified by placing a beam splitter behind the thermoplastic plate and taking pictures of the interferograms using a 35 mm SLR camera, while still recording on the VCR. A sequence of such interferograms showing the final stages of failure of a type A specimen is shown in Fig. 8. The fringes on the top half of the pictures display a continuous variation in w. Further, the fringe gradient is seen to decrease rapidly away from the hole edge. A fringe count of frame 3 reveals a change in the normal displacement at the hole edge of 10 μm. These pictures display a superior resolution to those recorded via the TV monitor. However, to adopt this method for the entire duration of a test was just too time consuming. It is thus important to compare these fringe records with those determined with the aid of the video recorder. It is seen that the areas in which the video-recorded fringes were unresolvable earlier can now readily be extrapolated from the areas in which the fringes are clearly resolvable. In Fig. 8(a), it is also seen that a surface buckle has already formed in the lower half of the specimen within a distance of approximately half a hole radius. The complete sequence (a)–(d) depicts the formation of the buckle in the upper half of the specimen which is found to be the last event prior to catastrophic failure. These pictures were taken with an exposure time of approximately 1 s and with a duration between frames of approximately 2–3 s.

Bearing in mind this information derived from the surfaces of the specimen, we now turn to a consideration of sectioning studies following the tests. In Fig. 9 are shown typical C-scan maps of damaged specimens. The extent of the damaged area depends on the load at which the specimen was unloaded, as given in Tables 2 and 3. Sectioning through the

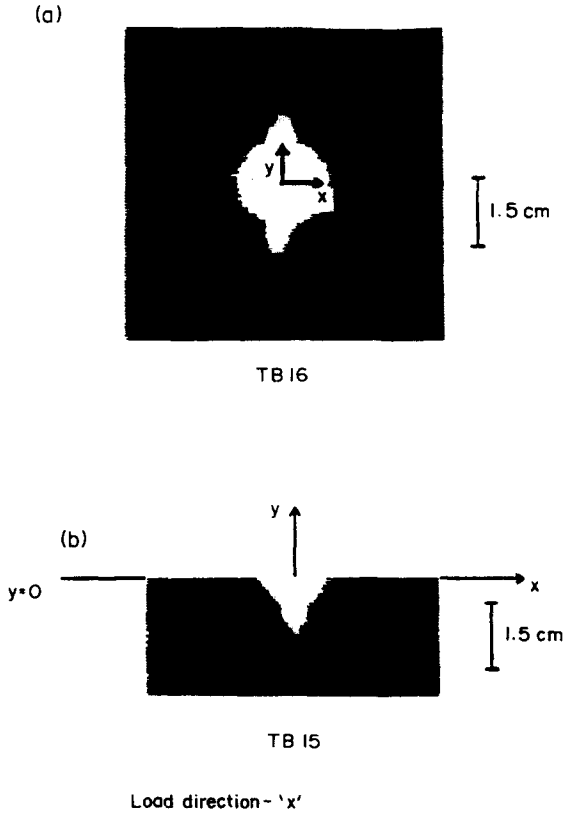

Fig. 9. C-scan maps of damaged specimens. (a) Specimen TB16. (b) Specimen TB15.

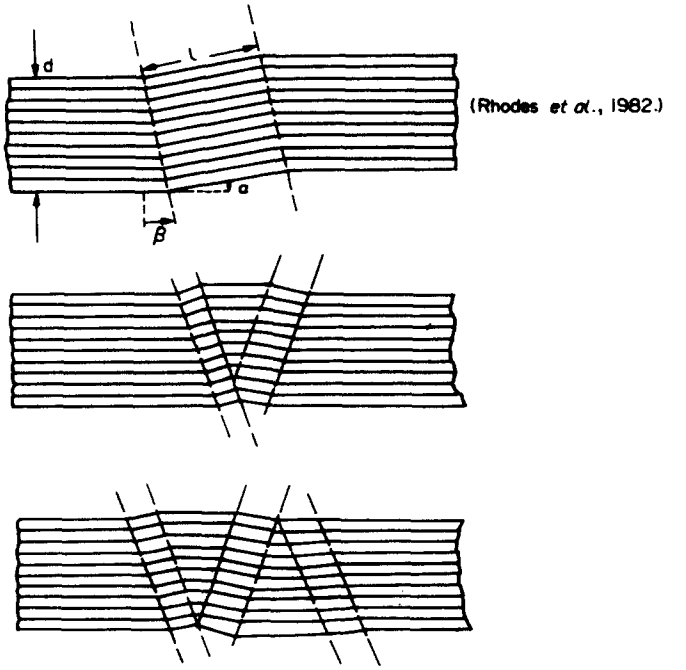

Fig. 10. Geometry of kink bands.

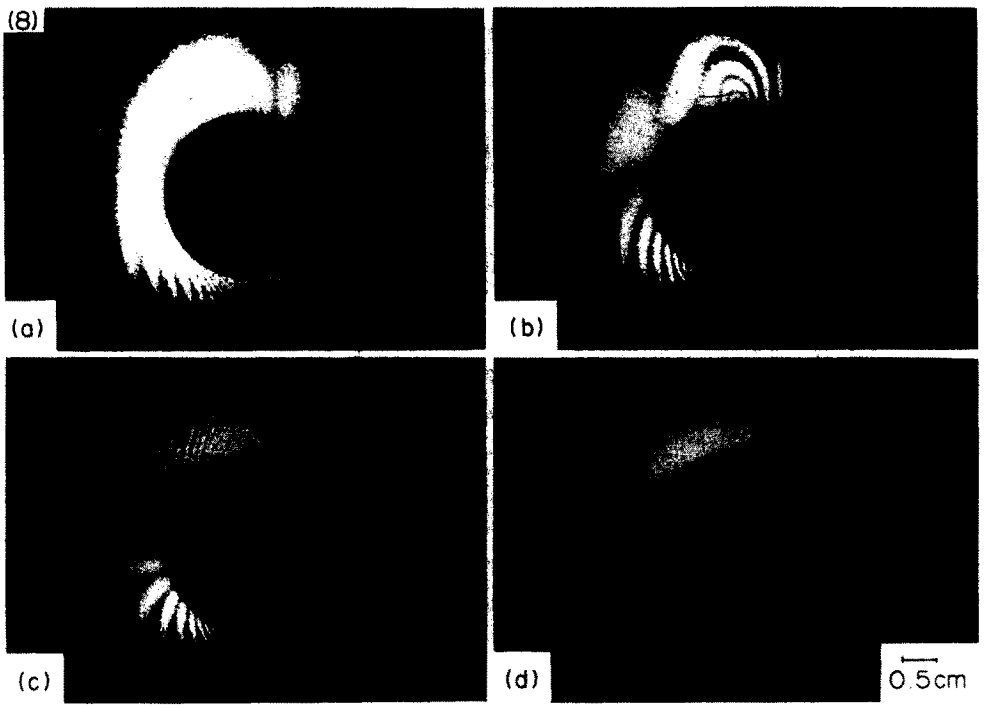

Fig. 8. Growth of surface delamination leading to catastrophic failure (specimen TB1).

damaged area and observation under an optical microscope revealed several narrow zones of fiber breaks within the 0° layers and inclined to the fiber orientation, to which we refer as fiber kink bands. The geometry of the kink bands is sketched in Fig. 10; the notation used by Evans and Adler (1977) to describe a typical kink band is also included. The kink bands were inclined at $\approx 65°$ to the load-carrying direction. The lengths of the fibers in the inclined zone measured 50–84 μm. It should be noted that the regions between the inclined zone appeared undamaged and remained oriented parallel to the fiber direction. In the study by Evans and Adler (1977) carbon fiber bundles of width ~ 400 μm oriented in three orthogonal directions were set in a graphite matrix and subjected to localized impact. Typical kink orientation angles were reported as (cf. Fig. 10 for notation) $\alpha \approx 45°$–$60°$ and kink boundary orientation β obeying $\beta \approx \alpha/2$ for broad $[(l/\mathbf{d}) \geqslant 0.1]$ kinks. For narrow kinks β was found to increase and α to be random. Corresponding results in our study which fall into the category $(l/\mathbf{d}) \geqslant 0.1$ indicate $\beta \approx 25°$–$30°$ and $\alpha \approx 15°$–$30°$. However, no definite trend between α and β could be established.

3.3. *Summary of common features of failure for type A and B specimens*

In this section we summarize the results presented so far and attempt to identify features that are common to types A (42% 0° plies) and B (8.3% 0° plies) laminates.

In both types A and B, the failure is initiated in a 0° ply at the hole edge and at the location of the maximal compression stress. In type A specimens, more 0° fiber failure occurs with simultaneous surface delamination buckling. These events occur very close to the catastrophic failure load. In type B specimens, subsequent to 0° fiber failure which occurs at around 75% of the ultimate failure load, gradual development of delamination cracking is observed, with the outermost delaminated sections undergoing buckling. In both types, the delaminations are seen to grow with increasing load. When the delaminated portions grow to a critical size, approximately on the order of 75–100% of the hole radius, an accelerated growth of the delaminations is observed and the specimens fail catastrophically.

The mechanics of the 0° fiber failure, which first becomes evident at the hole edge and is captured by the interferometer, consists of local microbuckling/fiber kinking. In order to elucidate the development and growth of the delaminations, it was desirable to study a laminate with a simpler stacking sequence than those exhibited by types A and B while still possessing similar ply orientations. The objective was to reduce the number of different interfaces (i.e. an interface between two dissimilar plies), but still maintain the overall laminate thickness. Thus, each ply group was clustered into groups of six, as indicated also in Table 1.

3.4. *Type C specimens*

This type of specimen contains 25% of the 0° plies. The interferometric patterns displayed by these specimens are typical of those observed earlier [cf. Figs 4(a)–4(d)]. However, inspection of the photomicrographs revealed that damage occurred on the hole surface which did not engender any anomaly in the interferometric out-of-plane response. This observation indicates that fiber damage at the hole surface did not necessarily give rise to localized bulging as detected by the interferometer before. To investigate this further, several specimens were loaded up to pre-determined levels of applied load, but unloaded prior to any detectable damage on the interferometer. A careful examination of the hole surface under an optical microscope was carried out next. This examination revealed the typical jutout failure as noticed before for specimen types A and B. Next, the specimen was sectioned at a distance 0.5 mm away from the hole edge, and inspected under an optical microscope. This inspection showed no damage to the 0° ply cluster. Thus, fiber jutout failure in these specimens develop gradually with a few layers of surface fibers participating. Next, as the external load reaches a critical value 0° fiber microbuckling occurs, and this damage propagates away from the edge of the hole. This process introduces a zone of damaged fibers within the 0° plies, which in turn causes the $(+45/-45)$ plies immediately next to this zone to bulge out of the plane. This deformation is then picked up through the interferometer. As the loading proceeds, the damaged area spreads in the form of planar

(XY plane) delamination cracks, causing local buckling of delaminated ply groups. Photomicrographs of the cutout surface for the events just described are shown in Fig. 11.

3.5. *Type D specimens*

The 0° ply percentage of these specimens are the same as for type C (25%) but now the 0° plies are located centrally in the laminate. The sequence of events leading to failure is similar to that described for the type C specimens, excepting the specimens IM12 and IM14 (see Table 3). These latter specimens failed abruptly without prior indication of fiber microbuckling. Inspection of the photomicrographs for these specimens indicated that the fiber jutout failure on the hole surface developed gradually.

Figure 12 shows a series of photomicrographs demonstrating the gradual development of failure in specimen IM23. Notice that subsequent to the 0° ply failure at 128.8 kN, delamination cracking within the 0° ply cluster is observed. To investigate the spreading of these delaminations and the extent of the propagating microbuckling failure, the specimen was unloaded from a load of 150.1 kN. Next, this specimen was C-scanned and the damaged area was found to extend out to about 75% of the radius of the hole. This specimen was then mechanically polished, sectioned and inspected under an optical microscope. The results of this examination are shown in Fig. 13. The narrow zone of local fiber failure in the XY plane extends outwad from the hole edge [Fig. 13(a)]. Notice the large fiber rotations in the XY plane in Fig. 13(b).

In order to assess the size of the damage zone, the specimen was sectioned at different locations and photomicrographs were obtained through a scanning electron microscope. These are shown in Fig. 14. A narrow zone of damaged fibers that runs across the entire thickness of the clustered midplane 0° plies (12 of them) at section A–A (see line drawing) is shown at the left of Fig. 14. The average width of this zone is approximately 58.5 μm (or 12 fiber diameters). The SEM photos at different sections also show that the fibers have undergone undulations that form themselves as inclined bands of broken fiber segments. The photograph designated "F" is a magnified view of section C–C (see insert in photograph of section C–C). Following the notation introduced in Evans and Adler (1977), which is indicated in Fig. 10, it is found that, for the kink band shown in Fig. 14, $(l/\mathbf{d}) \approx 12$, while $\alpha = 84°$ near the lower end marked "E" and $\beta = 9°$. Near the end "D", $\alpha = 72°$, while $\beta = 12°$. From the SEM photos at different sections, it is seen that the damage zone extent is ≈ 32 μm at section G–G, and 35 μm at section B–B. With a fiber diameter of 5 μm, the damage zone width (synonymous with "l" marked in Fig. 10) is found to be approximately $(l/\mathbf{d}) \approx 7$, implying a short wavelength instability.

3.6. *Summary of experimental findings*

The 0° ply microbuckling/kinking which occurs both in plane (XY) as well as out of plane (XZ), is found to originate at the hole surface and persist well into the interior of the specimen. This causes a narrow zone [$(l/\mathbf{d}) \approx 7$–12] within the 0° plies to lose structural integrity. Continuous viewing of the recorded videotapes shows the surface manifestation of this event as a well-defined cluster of fringes originating at the hole edge and propagating rapidly away from the hole.

Some of the IM series of specimens were provided with surface strain gages. From these strain gage measurements, it was found that the microbuckling failure for IM materials originated at a local strain level of ≈ 8500 μstrain, measured at the hole edge. The origination of fiber kinking at a free edge and its subsequent propagation into the interior of the structure has been reported before in a different context. We cite here the work of Chaplin (1977) and Hahn and Williams (1984).

The initiated damage leads to the formation of delamination cracks. The through-thickness locations of these are found to depend on the position of the 0° plies as shown on the photomicrographs. In type A specimens, the initiation event leads immediately to delamination buckling/growth resulting in complete failure. In type B specimens, the delaminated portions undergo an initial phase of slow growth/buckling until a critical area size is reached, when a rapid stage of further growth/buckling leads to catastrophic failure. In types C and D specimens, the failure is similar to that of type B.

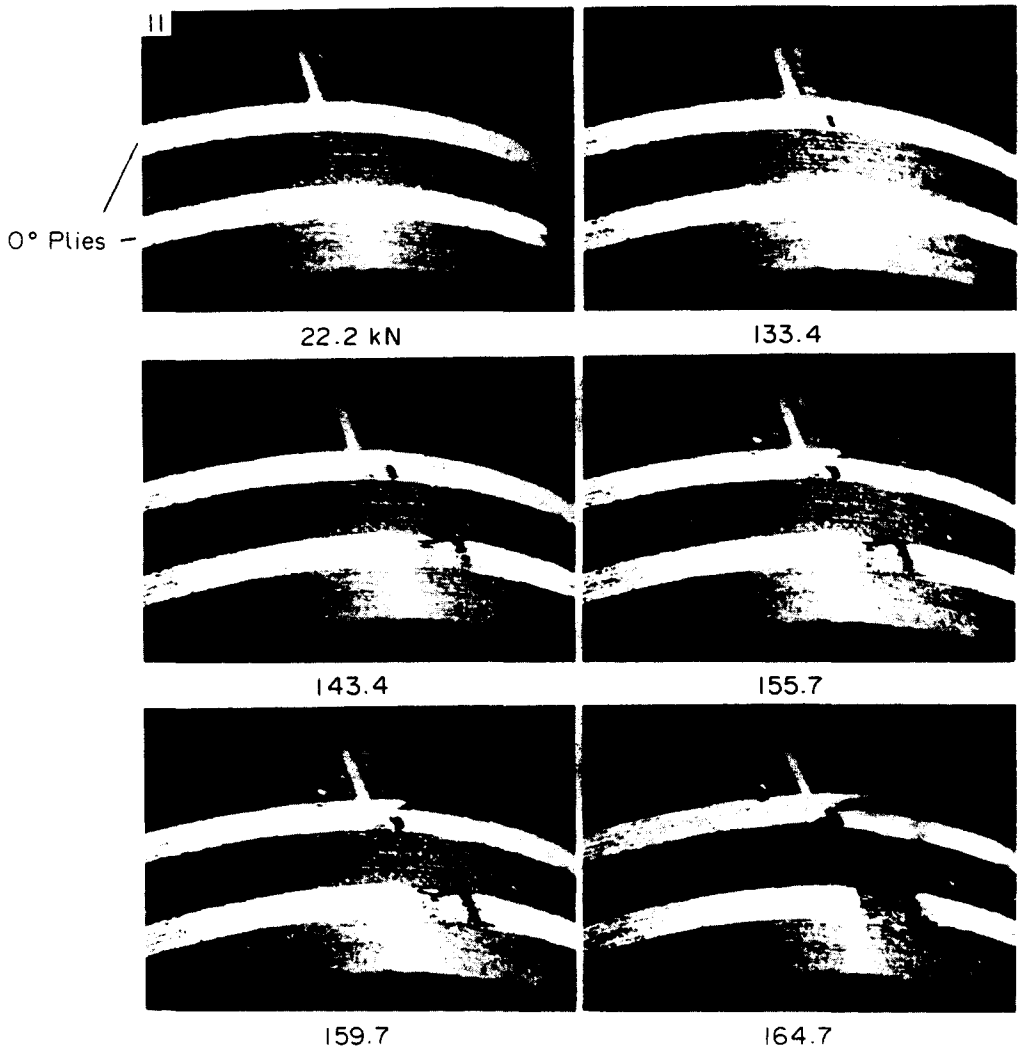

Fig. 11. Hole surface photomicrographs of specimen IM26 (type C).

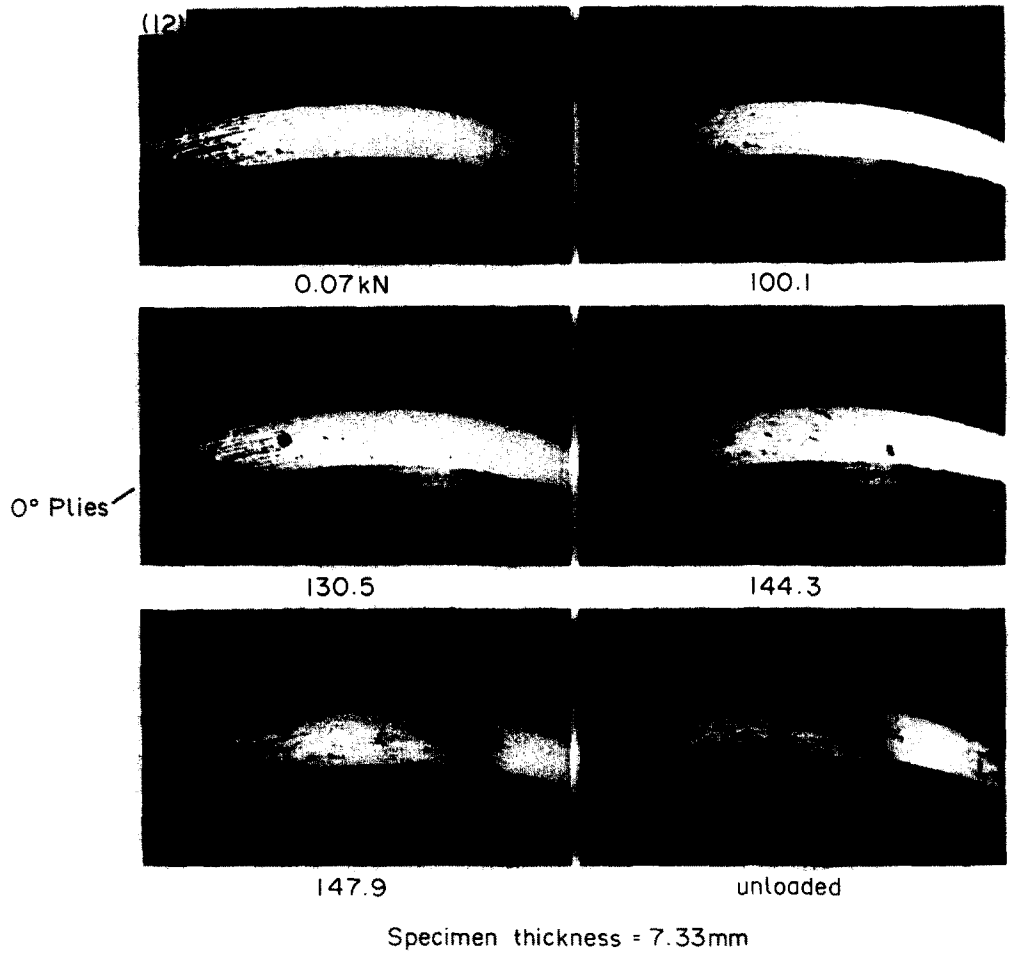

Fig. 12. Hole surface photomicrographs of specimen IM23 (type D).

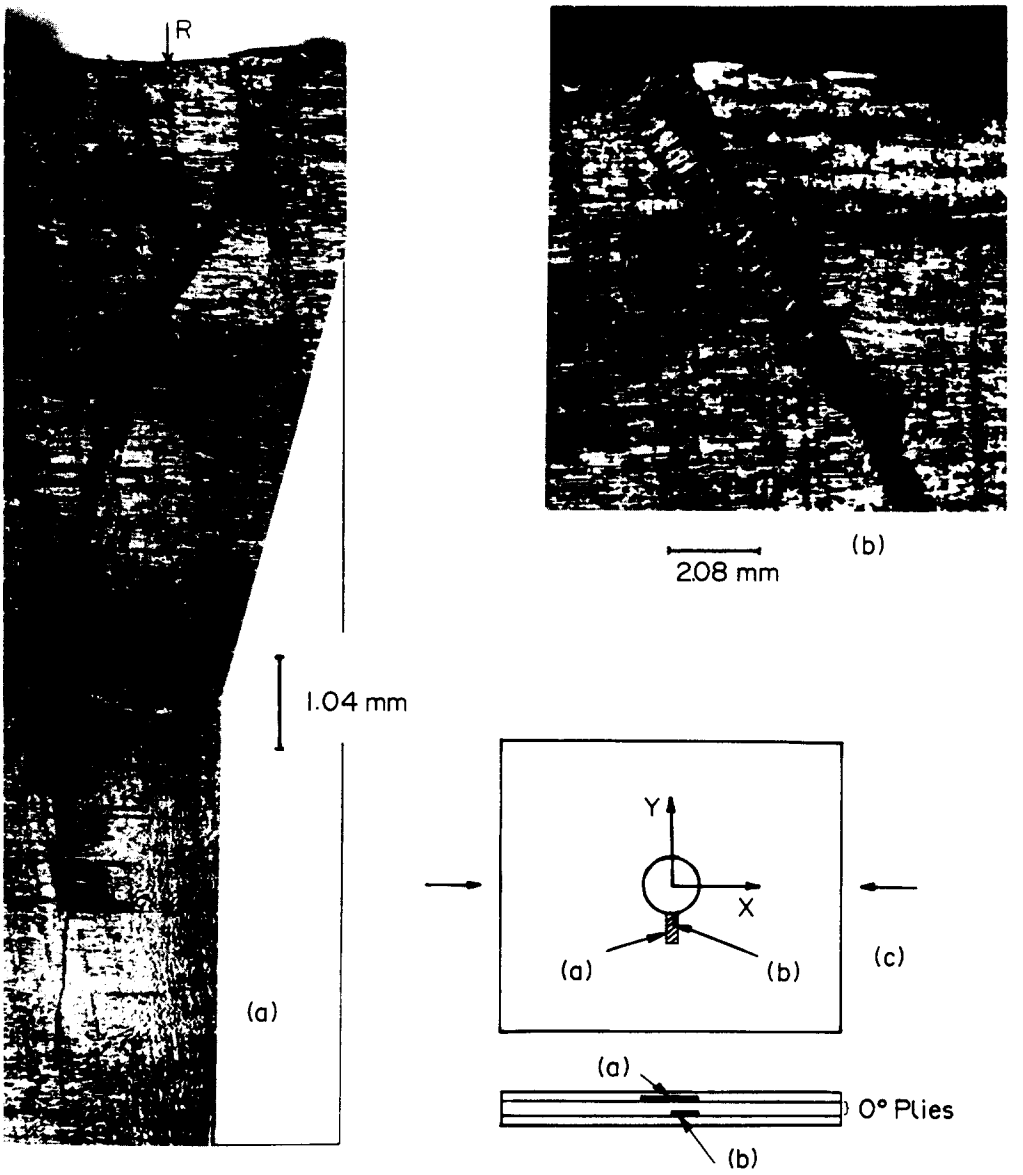

Fig. 13. Internal damage in the vicinity of the hole (specimen IM23): (a) view of 0° layers; upper edge is the hole boundary R; (b) location in upper right hand corner of (a), but in a different layer than (a); (c) map of damage areas (a) and (b).

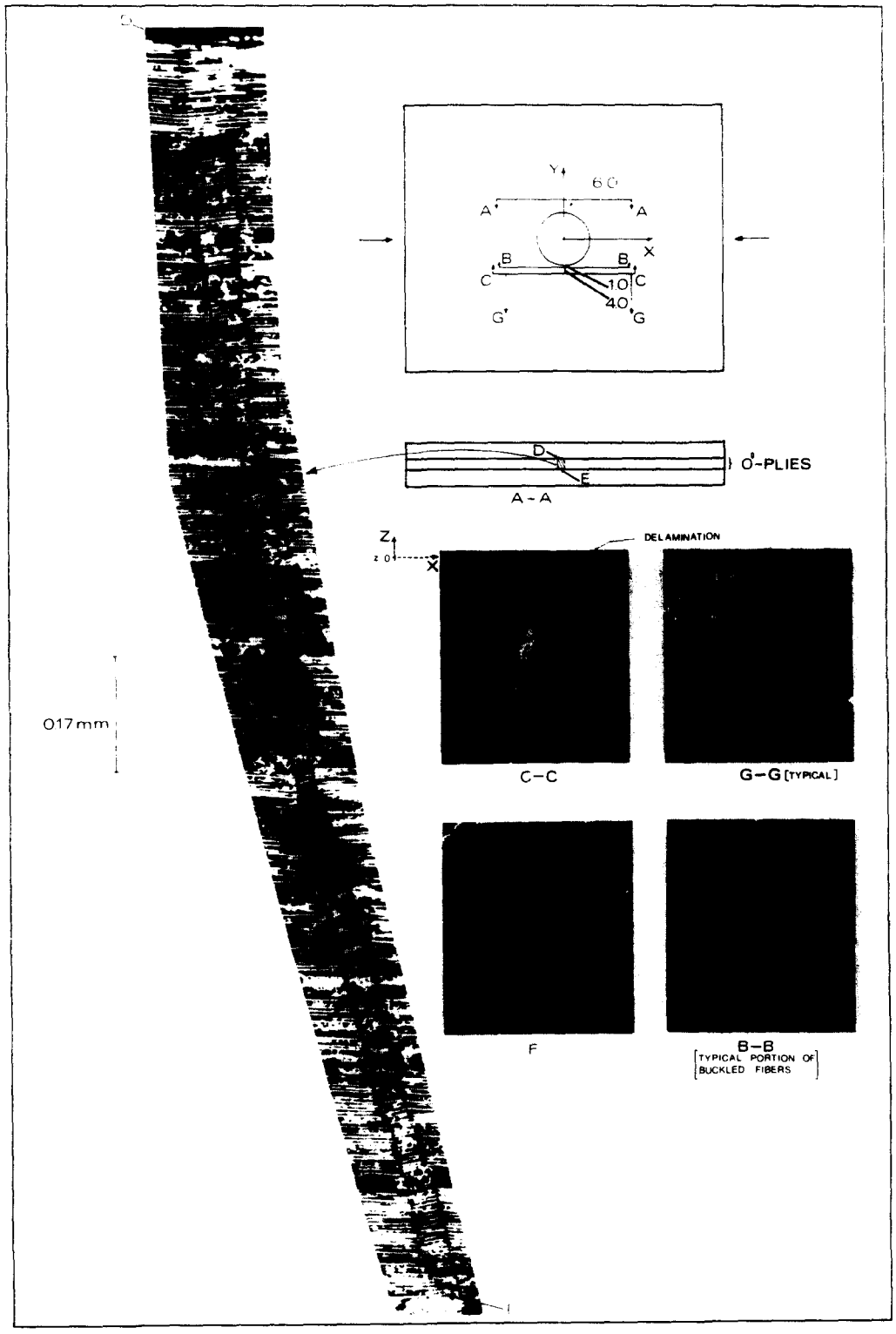

Fig. 14. Scanning electron photomicrographs of internal damage at the vicinity of the hole (specimen IM23).

Table 4. Averaged initiation and final failure loads for IM series specimens

Type	Zero ply %	No. of specimens (N)	P_i Mean P_i	σ_x	$\sigma_x/\sqrt{N}$	No. of specimens (N)	P_f Mean P_f	σ_x	$\sigma_x/\sqrt{N}$
A	42	8	126.5	4.6	1.6	6	135.7	5.9	2.4
B	8	7	68.5	4.2	1.6	4	92.1	4.1	2.0
C	25	5	85.1	2.8	1.2	4	92.1	0.9	0.4
D	25	4	74.4	1.4	0.7	3	91.0	3.7	2.1

Standard deviation $\sigma_x = \sqrt{\frac{1}{N-1}\sum_{i=1}^{N}(x_i-\bar{x})^2}$.
Standard deviation of the mean $\equiv \sigma_x/\sqrt{N}$.

From the table of results presented for the IM series (see Table 3), where the results for the "small" specimens have been grouped according to type, the average initiation and failure loads can be calculated. These are presented in Table 4. Since some specimens were unloaded prior to final failure, the number of data points used to compute P_f is less than that for P_i. A similar procedure was not followed for the larger specimens, as data for the type "AL" is lacking. This is so because this laminate demands high load values at failure (the table top compression device has a maximum load capacity of 222 kN) which are in excess of the capacity of the loading device. From the results in Table 4, it is seen that the load-carrying capacity of a laminate is dictated by the 0° ply percentage within the laminate. Indeed, a larger percentage of 0° plies leads to a "stiffer" laminate which fails in a "brittle" fashion (initiation and final failure loads are close to each other). As the percentage of 0° plies is reduced, the laminate is seen to fail in a "ductile fashion" (initiation and final failure are not close, the failure process being also dictated by the percentage of 0° plies). Thus, we see that beyond failure initiation by microbuckling, the delamination and buckling/growth phase is influenced by the overall laminate stiffness.

However, common to all the laminates tested in this investigation is the level of localized strain at which damage initiation occurs. This initiation strain can be used as a useful design guide, since for all practical purposes, once 0° ply failure has occurred, it is reasonable to deem the laminate as being unsafe. A mechanical model for the initiation problem is presented in Waas *et al.* (1989).

Acknowledgements—This research was supported by the National Aeronautics and Space Administration under Grant NSG-1483. The authors are appreciative of this support. The interest and encouragement of Dr James H. Starnes, Jr, NASA Langley, in pursuing this work is gratefully acknowledged. The invaluable support through donation of optical equipment by the Newport Research Corporation is much appreciated.

REFERENCES

Budiansky, B. (1983). Micromechanics. *Comput. Struct.* (16) (1–4), 3–12.
Chaplin, C. R. (1977). Compressive fracture in unidirectional glass reinforced plastics. *J. Mat. Sci.* **12,** 347–352.
Evans, A. and Adler, A. 1977). Kinking as a mode of structural degradation in Carbon fiber composites. *Acta Metall.* **26,** 725–738.
Hahn, H. and Williams, J. G. (1984). Compression failure mechanisms in unidirectional composites. NASA TM 85834.
Knauss, J., Starnes, J. and Henneke, E. (1978). The compressive failure of Gr/Epoxy plates with circular holes. NASA CR 157115, N78-24295.
Mikulas, M. (1980). Failure prediction techniques for compression loaded composite laminates. NASA CP 2142.
Owners Manual HC300,301 (1986). Newport Research Corporation, CA, U.S.A.
Pfaff, R. D. (1986) Private communication. Caltech, Pasadena, CA.
Rhodes, M., Mikulas, M. and McGowan, P. (1982). Effect of orthotropic properties and panel width on the compression strength of Gr/Epoxy laminates with holes. AIAA paper No. 82-0749.
Shuart, M. J. and Williams, J. G. (1986). Compression behavior of [+45/−45] dominated laminates with a circular hole or impact damage. *AIAA Jl* **24,** 115–222.
Starnes, J. and Williams, J. G. (1982). Failure characteristics of Gr/Epoxy structural components loaded in compression. NASA TM 84552.

Vest, C. M. (1979). *Holographic Interferometry*. Wiley, New York.
Waas, A. (1988). Compression failure of fibrous laminated composites in the presence of stress gradients: experiment and analysis. Ph.D. thesis, Caltech, Pasadena, CA.
Waas, A., Babcock, C. D. and Knauss, W. G. (1989). A mechanical model for elastic fiber microbuckling. *ASME Proc. Composite Material Technology* (Edited by D. Hui and T. J. Kosik), PD-**24**, 203–215.